

Coupling of ecosystem-scale plant water storage and leaf phenology observed by satellite

Feng Tian^{1,2*}, Jean-Pierre Wigneron^{3*}, Philippe Ciais⁴, Jérôme Chave⁵, Jérôme Ogée³, Josep Peñuelas^{6,7}, Anders Ræbild², Jean-Christophe Domec⁸, Xiaoye Tong², Martin Brandt², Arnaud Mialon⁹, Nemesio Rodriguez-Fernandez⁹, Torbern Tagesson^{1,2}, Amen Al-Yaari³, Yann Kerr⁹, Chi Chen¹⁰, Ranga B. Myneni¹⁰, Wenmin Zhang², Jonas Ardö¹ and Rasmus Fensholt²

Plant water storage is fundamental to the functioning of terrestrial ecosystems by participating in plant metabolism, nutrient and sugar transport, and maintenance of the integrity of the hydraulic system of the plant. However, a global view of the size and dynamics of the water pools stored in plant tissues is still lacking. Here, we report global patterns of seasonal variations in ecosystem-scale plant water storage and their relationship with leaf phenology, based on space-borne measurements of L-band vegetation optical depth. We find that seasonal variations in plant water storage are highly synchronous with leaf phenology for the boreal and temperate forests, but asynchronous for the tropical woodlands, where the seasonal development of plant water storage lags behind leaf area by up to 180 days. Contrasting patterns of the time lag between plant water storage and terrestrial groundwater storage are also evident in these ecosystems. A comparison of the water cycle components in seasonally dry tropical woodlands highlights the buffering effect of plant water storage on the seasonal dynamics of water supply and demand. Our results offer insights into ecosystem-scale plant water relations globally and provide a basis for an improved parameterization of eco-hydrological and Earth system models.

Water stored in plant tissues participates in physiological and biochemical processes (for example, metabolism and nutrient/sugar transport) and sustains the integrity of the plant hydraulic system by buffering the imbalance between transpirational water loss and root-soil water uptake^{1,2}. Water movement in plants is a passive process, following a gradient of water potential (from higher to lower) generated by transpirational demand (regulated by stomata)³ and different solute concentrations between cells (osmosis)⁴. In response to changes in environmental conditions and metabolic activities, plant water storage varies from diurnal to seasonal timescales as a function of plant structure and hydraulic strategies^{5–7}. Studies on the dynamics of plant water storage typically use measurements of sap flow hysteresis and leaf water potential on individual trees over relatively limited periods^{7–10}. Scaling up tree-level data to the ecosystem scale is challenging due to the high spatial heterogeneity of plant composition and soil properties, thus precluding large-scale (continental or global) estimates of the dynamics of plant water storage.

Satellite passive microwave radiometers sense the natural Earth surface thermal emission at wavelengths of 0.1–30 cm from both the soil and vegetation layers, quantified as brightness temperature. The vegetation layer is semi-transparent, attenuating the microwave radiations passing through, and creating a vegetation optical depth (VOD) proportionally linked to the vegetation water content (kg m^{-2})^{11,12}. The higher the microwave frequency, the stronger the vegetation attenuation effect. The low-frequency L-band (1.4 GHz) VOD (L-VOD) can detect changes in plant

water storage even for dense forest canopies^{13–15}, where the woody tissues of stems and branches hold most plant water¹⁶. This detection is not possible with VOD products at higher frequencies (>6 GHz), because their signals are dominated by the water status of canopy leaves^{13,14,17–19}. Satellite-based VOD retrievals from X-band (10.7 GHz) observations over the day and night have recently been used to map ecosystem-scale anisohydricity—an indicator of stomatal and xylem regulation on water use^{20,21}. Since 2010, the first satellite-based L-band radiometer carried by the Soil Moisture and Ocean Salinity (SMOS) mission²² further has enabled global-scale monitoring of the dynamics in plant capacitive water storage, which is another key functional trait in forest eco-hydrological processes.

Here, we used the SMOS L-VOD product^{23,24} as a proxy for time and space variations in ecosystem-scale plant water storage, and examined its seasonal dynamics globally over the period 2011–2016. Since leaf area scales the transpirational flux and photosynthetic productivity, we also examined the coupling between seasonal variations in L-VOD and leaf phenology (defined as the seasonality of the satellite-observed leaf area index (LAI)).

Results and discussion

Seasonal amplitude of L-VOD. We analysed the seasonal dynamics of ecosystem-scale plant water storage by concatenating six-year (2011–2016) SMOS L-VOD data into a mean yearly daily time series at a spatial resolution of 0.25° (Methods and Supplementary Fig. 1). Large land regions had substantial data gaps due to the influence of

¹Department of Physical Geography and Ecosystem Science, Lund University, Lund, Sweden. ²Department of Geosciences and Natural Resource Management, University of Copenhagen, Copenhagen, Denmark. ³INRA, UMR 1391 ISPA, Bordeaux, France. ⁴Laboratoire des Sciences du Climat et de l'Environnement, CEA/CNRS/UVSQ, Gif-sur-Yvette, France. ⁵UMR 5174 Laboratoire Evolution et Diversité Biologique, Université Paul Sabatier, CNRS, Toulouse, France. ⁶CSIC, Global Ecology Unit CREAM-CSIC-UAB, Bellaterra, Spain. ⁷CREAF, Cerdanyola del Vallès, Spain. ⁸Bordeaux Sciences Agro, UMR 1391 INRA-ISPA, Gradignan, France. ⁹CESBIO, Université de Toulouse, CNES/CNRS/IRD/UPS, Toulouse, France. ¹⁰Department of Earth and Environment, Boston University, Boston, MA, USA. *e-mail: ftian2012@gmail.com; jean-pierre.wigneron@inra.fr

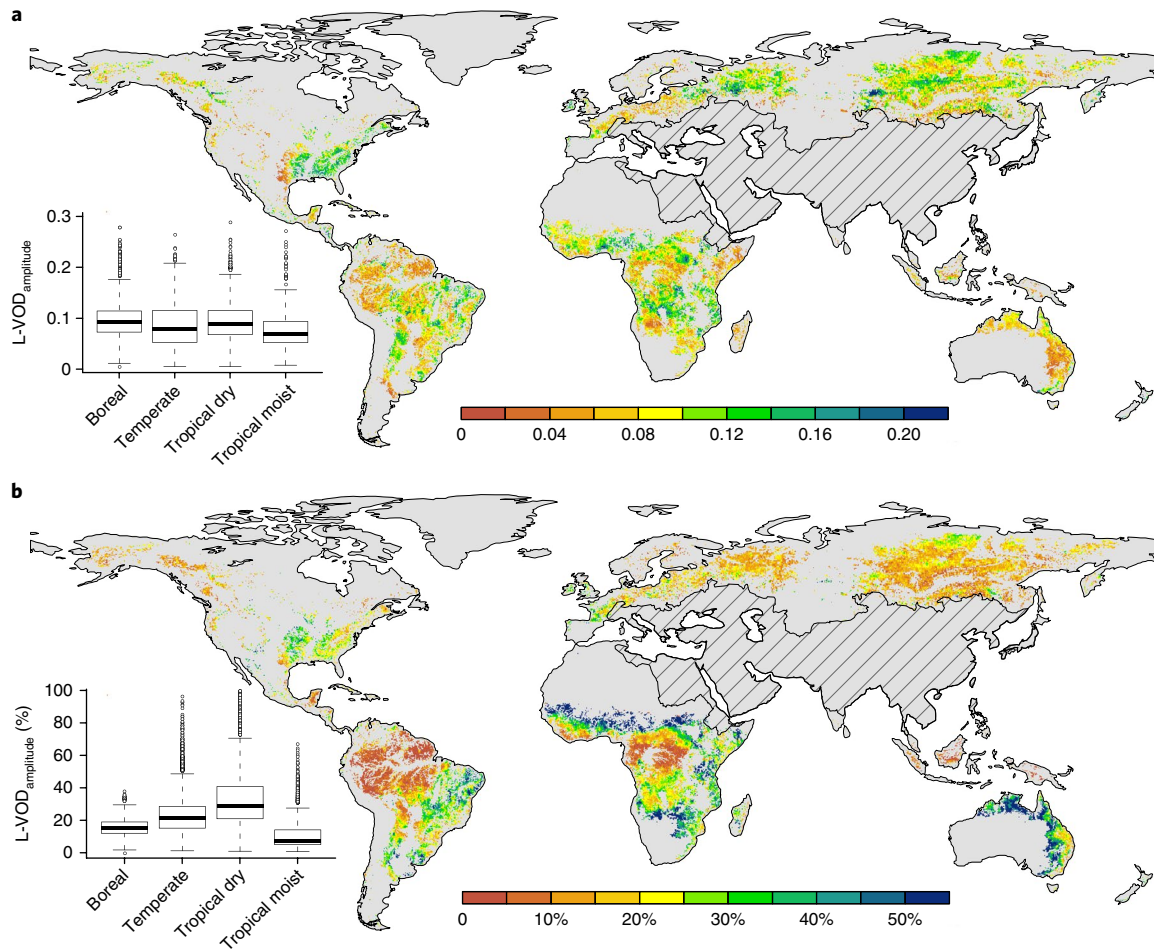


Fig. 1 | Seasonal amplitude of L-VOD. a, Absolute seasonal amplitude of L-VOD. **b**, Relative seasonal amplitude of L-VOD normalized by the annual maxima. The inserted whisker plots were calculated for unfiltered pixels in four regions; that is, boreal ($n=12,880$), temperate ($n=6,775$), tropical dry ($n=14,152$) and tropical moist ($n=7,737$). The lower and upper box edges correspond to the 25th and 75th percentiles. The whiskers extend from the box edges by $1.5\times$ the interquartile range (IQR), which is the distance between the 25th and 75th percentiles. Areas with substantial data gaps or seasonal inundation, and ecoregions not considered in this study were filtered out and are shown in grey. Areas influenced by RFI are marked with hatching.

radio frequency interference (RFI) on the SMOS signal²⁵ (mainly in Asia; Supplementary Fig. 2), open water bodies and a lack of data retrievals from frozen soil in the northern latitudes during the cold season. We therefore restricted our analysis to pixels with continuous L-VOD data over 120 d and focused on four regions representing various biomes of contrasting ecosystem functioning—boreal, temperate, tropical dry and tropical moist—based on a map of terrestrial ecoregions²⁶ (Supplementary Fig. 3). To ensure a high accuracy of the L-VOD seasonal patterns, we excluded areas with sparse vegetation cover where the tree cover fraction was below 5%²⁷ and areas that were seasonally inundated²⁸; that is, $>5\%$ area covered by flooding within an L-VOD pixel.

Globally, the annual maximum L-VOD was highly correlated with the distribution of tree cover fraction and tree height (Supplementary Fig. 4)^{29,30}. The absolute peak-to-peak seasonal amplitude of the mean L-VOD time series was similar (within 0.3 L-VOD units) among the four regions (Fig. 1a), even though plant productivity in these regions is controlled by different climate variables (for example, temperature, water and radiation) and nutrient limitations. However, the L-VOD seasonal amplitude relative to the annual maxima differed significantly among regions (Fig. 1b), and was largest in the tropical dry region ($>30\%$ on average) and smallest in the tropical moist region ($<10\%$ on average), with temperate and boreal regions having intermediate values.

Seasonal coupling of L-VOD and LAI. Water stored in plant tissues and its seasonal dynamics differ substantially across vegetation life-forms (for example, woody versus herbaceous plants). Herbaceous plants are usually annuals, so the seasonal amplitude of herbaceous water storage is determined primarily by the amount of foliage in the growing season. In contrast, trees store most of their water in woody tissues, with water-holding capacities varying among functioning tissues^{16,31}. Also, determining the dynamics of water storage is more complex for woody than herbaceous plants because trees may access deep soil water and have more sophisticated hydraulic strategies^{32–34}. We examined the spatial relationships between the absolute seasonal amplitudes of L-VOD and LAI in each of the four regions. As expected, linear correlations between the two signals were higher in areas with limited tree cover (5–10%) ($R\approx 0.56$, $P<0.05$; Fig. 2), except in the boreal region ($R=0.24$, $P<0.05$) where data gaps in winter may cause a partial loss of information in the transitional period between winter and spring/autumn. However, the seasonal amplitudes of L-VOD were positively correlated with LAI across space for areas with high tree cover ($>60\%$) in the boreal ($R=0.35$, $P<0.05$) and temperate ($R=0.32$, $P<0.05$) regions, but the relationship was much lower in the tropical moist ($R=0.09$, $P<0.05$) region and not significant ($R=-0.02$, $P>0.05$) in the tropical dry region. These findings suggest a lower influence of leaf fluctuations on the seasonal amplitude of plant water storage in tropical than boreal or temperate forests.

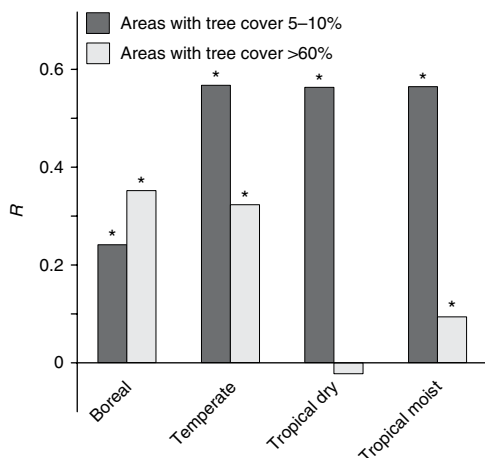


Fig. 2 | Relationship between seasonal amplitude of L-VOD and LAI.

Pearson correlation coefficients (R) for areas with tree covers of 5–10 and >60% within the four regions: boreal ($n=699$ and 4,193, respectively), temperate ($n=1,010$ and 1,236, respectively), tropical dry ($n=1,804$ and 1,704, respectively) and tropical moist ($n=237$ and 5,493, respectively). Significant correlations ($P < 0.05$) are labelled with asterisks. The scatterplots for each comparison are shown in Supplementary Fig. 5.

We then examined the seasonal synchronicity of plant water storage and leaf phenology by calculating the time lag that characterizes the maximum Spearman's rank correlation coefficient between L-VOD and LAI time series (for pixels with a clear seasonality in both indices; see Methods). The seasonal variations in L-VOD were highly synchronous with LAI in boreal and temperate regions ($R > 0.9$, $P < 0.05$), with time lags ranging from -30 to $+60$ d (Fig. 3a; positive values represent L-VOD peaks succeeding LAI). In contrast, the relationship was clearly asynchronous in tropical woodlands (for example, the woodlands around rainforests in the Congo Basin), with time lags up to 180 d (Fig. 3a). This time lag was found to follow an increasing gradient in L-VOD and tree cover in two African savannah and woodland regions (regions i and ii in Fig. 3a,b), but not in two other contrasted regions: one with wet summers in southeastern USA (region iii in Fig. 3a,b) and the other with dry summers in central Siberia (region iv in Fig. 3a,b). This suggests different strategies of the coupling between plant water storage and leaf phenology of trees in dry tropical woodlands compared with temperate and boreal forests.

The average seasonalities of L-VOD and LAI are shown in Fig. 3c for pixels with equivalent tree cover fractions (60–65%) from each selected region. The long L-VOD/LAI time lags in tropical woodlands caused an almost reversed seasonal pattern between the two signals (graphs i and ii in Fig. 3c). We further included the seasonality of a high-frequency X-band VOD (X-VOD)³⁵—a proxy for the water content of the upper canopy since X-band microwaves penetrate less than L-band microwaves. The seasonal peaks of X-VOD were between those of L-VOD and LAI (Fig. 3c), indicating high consistency among the independent satellite observations. Moreover, we performed a series of sensitivity analyses on the algorithm used to retrieve L-VOD to verify the robustness of the observed seasonal patterns in the tropical dry region (region i in Fig. 3a; see Methods and Supplementary Figs. 6, 7 and 8).

Seasonal water balance. Plants regulate water exchange between sub-soil layers and the atmosphere through soil water uptake and transpiration. We evaluated the role of plant water storage on the seasonal water balance at the ecosystem scale by analysing the development of various components of the water cycle, including plant water storage (L-VOD), the terrestrial groundwater storage anomaly

(TWS), surface soil moisture, rainfall and estimates of transpiration. The TWS integrates the groundwater from the soil surface to deep ground³⁶. Seasonal variations in TWS indicate the net balance between soil water input (for example, by rainfall) and consumption (for example, by evapotranspiration)³⁷. We calculated the seasonal time lag between L-VOD and TWS as was done for L-VOD and LAI. Large and spatially homogeneous time lags of about 120 and 90 d were obtained in the entire regions of southeastern USA and central Siberia, respectively (Fig. 4). In contrast, a highly varying time lag from 0 to around 90 d was found in the central southern African savannah/woodland region (the Miombo region), with increasing time lag following the gradient of increasing vegetation density (L-VOD and tree cover; Fig. 4). This indicates different roles of herbaceous and woody vegetation in the eco-hydrological processes in the Miombo region, whereas their roles are similar in southeastern USA and central Siberia.

To better illustrate the differences in the seasonal variations of plant versus soil water storage and water fluxes, we selected two sites with a $1^\circ \times 1^\circ$ spatial extent (16 L-VOD pixels) in the period 2011–2012 (Fig. 5): one in the US temperate forests (region iii of Figs. 3 and 4; centred at 33.5°N , 85.5°W) and one in the African Miombo woodlands (region i of Figs. 3 and 4; centred at 11.5°S , 18.5°E). For the US temperate forest site, rainfall and surface soil moisture were relatively stable throughout the year, whereas TWS exhibited clear seasonal fluctuations (Fig. 5a). TWS reached the lowest level by the end of growing season, then increased and peaked around the start of the growing season, followed by a continuous decrease during the growing season. Given the rather even water input from rainfall over time, the seasonal fluctuations in TWS are probably attributable to changes in evaporative demand enhancing water losses through transpiration and soil evaporation during summer. L-VOD was found to highly co-vary with LAI and transpiration rates, which may be explained by the requirements of abundant stem water storage to buffer xylem tension induced by transpiration³⁸.

In comparison, the Miombo woodlands site has distinct dry and rainy seasons (Fig. 5b). LAI began to increase several weeks before the onset of the rainy season, confirming the pre-rain green-up reported by previous studies³⁹. Surface soil moisture remained at the lowest level during the entire dry season, while TWS decreased continuously over this rain-free period, suggesting that deep groundwater was used by trees during the dry season⁴⁰. Transpiration generally co-varied with LAI seasonal variations. In contrast, L-VOD increased from the latter period of the rainy season until the beginning of the dry season, stayed high throughout the rain-free period and decreased when LAI increased again. Together, these results indicate a critical role of plant water storage in buffering the seasonal dynamics of water supply and demand, and sustaining fresh leaves formed before the rain in these tropical dry woodlands.

Endogenous whole-plant control of leaf phenology has been documented in some seasonally dry tropical tree species^{41,42}, where water stored in the stems directly contributes to leaf emergence during the pre-rain green-up period^{43,44}, which may explain the decrease in L-VOD at the end of the dry season. The cambium of Miombo trees grows and makes new vessels during a short period late in the rainy season^{45,46}, when L-VOD increases. The continued increase in L-VOD at the end of the rainy season and at the beginning of the dry season is consistent with the reduced loss of transpirational water associated with leaf shedding that enables the rehydration of stem tissues and the subsequent leaf emergence^{43,45}. The Miombo woodland region is the largest hot-spot area characterized by long time lags between L-VOD and LAI, but the northern African woodlands and Brazilian Cerrado have similar patterns as well (Supplementary Fig. 9).

The specific seasonal behaviour of various water cycle components within each region indicates the adaptation of plants to local climatic conditions (for example, seasonal variations in rainfall,

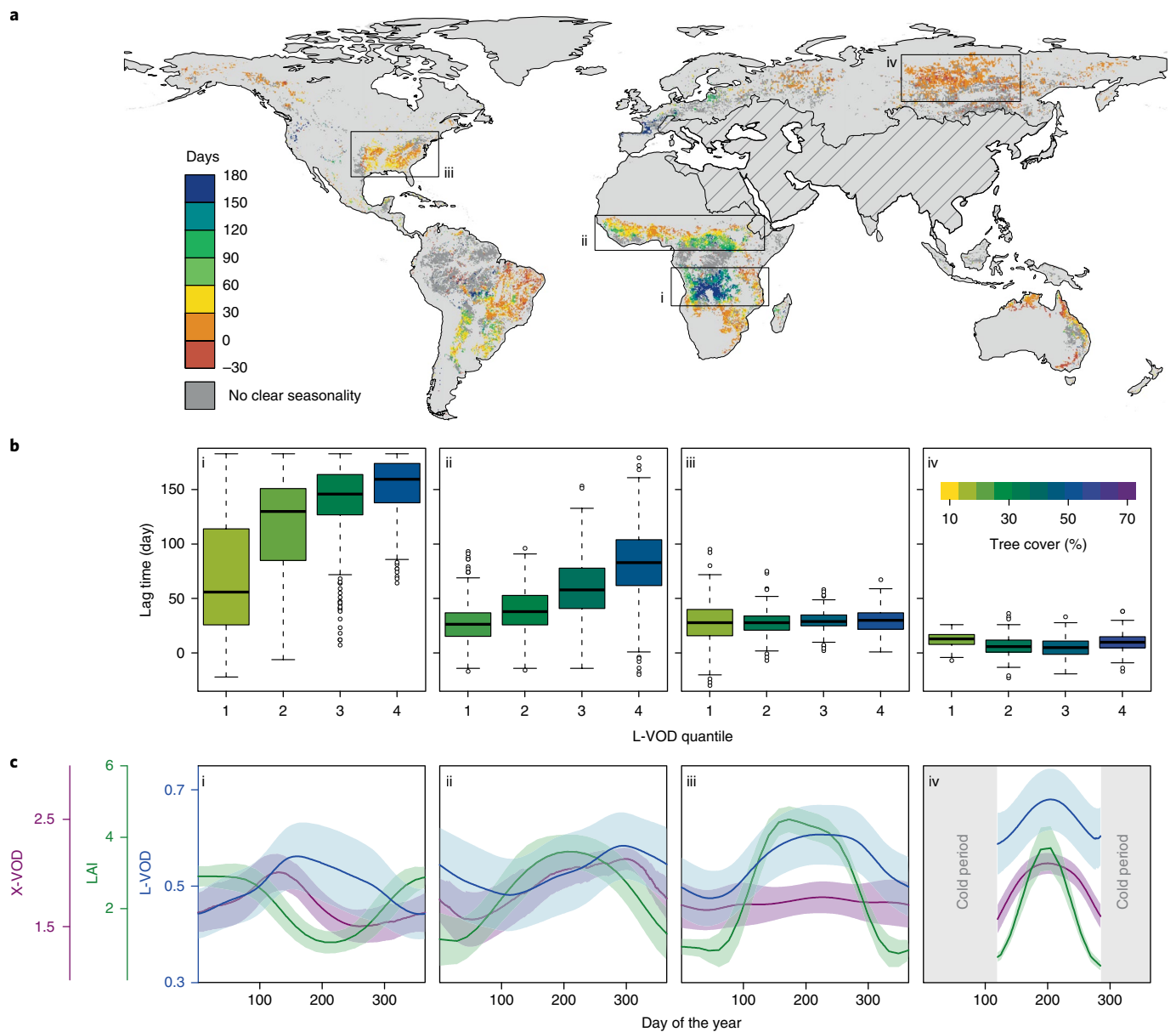


Fig. 3 | Temporal coupling between L-VOD and LAI seasonality. a, Lag time for L-VOD to obtain the highest correlation with LAI for pixels with clear seasonality. Areas influenced by RFI are marked with hatching. **b**, Spatial relationships between L-VOD/LAI lag time, annual maximum L-VOD and tree cover fraction for the four selected areas indicated in **a** by black rectangles. The lower and upper box edges correspond to the 25th and 75th percentiles. The whiskers extend from the box edges by 1.5 \times IQR. **c**, Seasonal curves of mean L-VOD, LAI and X-VOD for the pixels with a tree cover of 60–65% for the four selected areas ($n=152, 79, 124$ and 212, respectively, for regions i, ii, iii and iv). The shading represents s.d. No VOD values were retrieved during winter periods with frozen soils.

temperature and photosynthetic active radiation) and abiotic conditions (for example, soil types and soil water supply) at the ecosystem scale. The spatial heterogeneity in species composition needs to be considered for further in-depth hydrological and physiological interpretations of the large-footprint satellite signal because closely located tree species sharing the same environmental conditions can be characterized by different hydraulic strategies; for example, between soft wood species and hard wood species⁴³. At the same time, different species across ecosystems may have similar hydraulic mechanisms, as root hydraulic lift and redistribution of deep groundwater were identified in both temperate forest and tropical woodland ecosystems^{47,48}.

Our study provides observational evidence of global differences in the interaction between plant water storage and leaf phenology. The satellite-based L-VOD product allows for the efficient and

repeated monitoring of changes in large-scale plant water storage, which is highly valuable for mapping and understanding spatial differences in plant hydraulic strategies^{3,49}. Furthermore, the lag analyses between satellite-observed L-VOD and LAI/TWS, as well as the resulting spatial patterns in relation to vegetation density and types, provide a convenient way to condense patterns of plant water storage across the globe, which can be used to test and parameterize eco-hydrological and Earth system models. As the time series covered by L-band satellite microwave observations is expanding and the spatial coverage over RFI-influenced areas is being improved, the L-VOD product is providing a strong complement to the high-frequency VOD products and greenness-/productivity-oriented optical satellite records for studying continental-scale ecosystem responses to climate change.

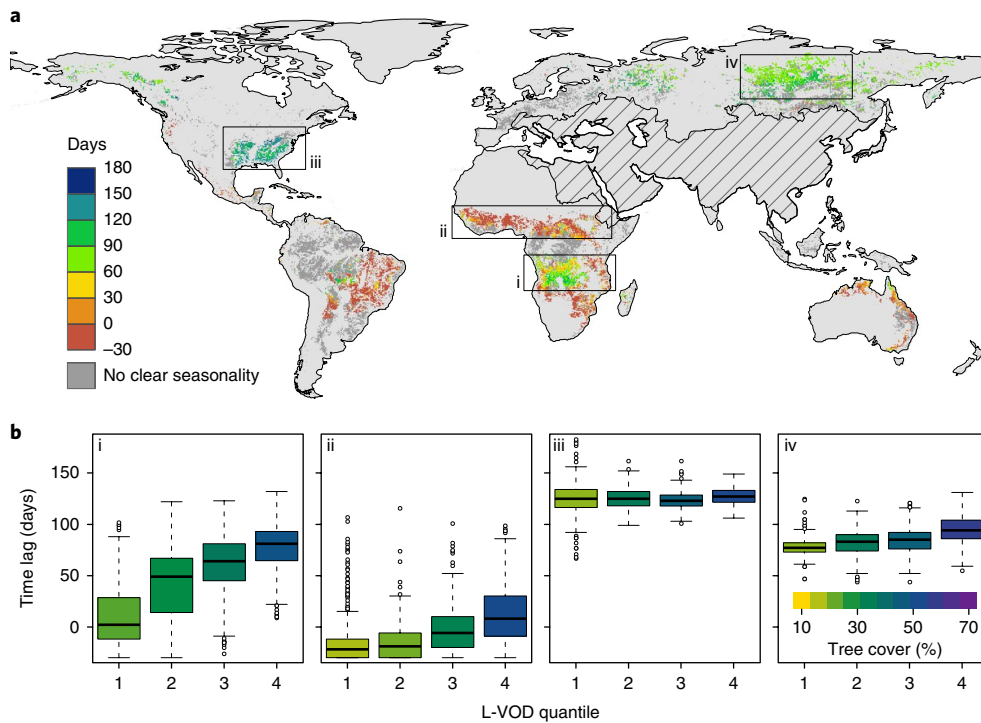


Fig. 4 | Temporal coupling between L-VOD and TWS seasonality. **a**, Lag time for L-VOD to obtain the highest correlation with TWS for pixels with a clear seasonality. Areas influenced by RFI are marked with hatching. **b**, Spatial relationships between L-VOD/TWS lag time, annual maximum L-VOD and tree cover fraction for the four selected areas indicated by black rectangles. The lower and upper box edges correspond to the 25th and 75th percentiles. The whiskers extend from the box edges by 1.5× IQR.

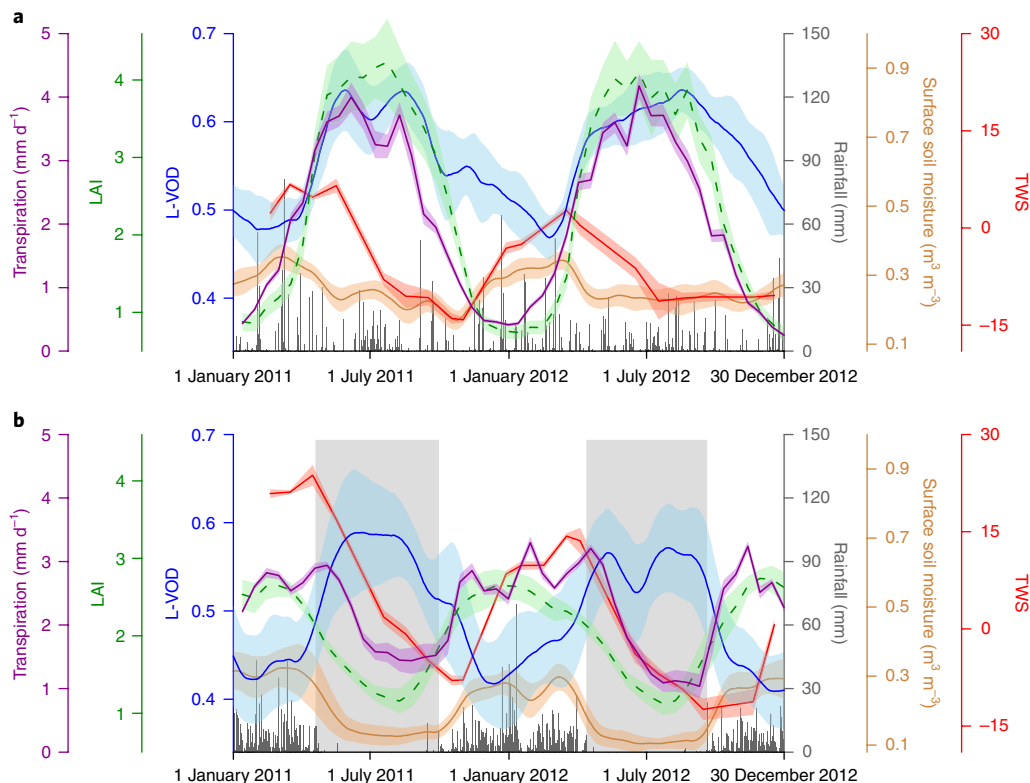


Fig. 5 | Seasonal water balance in two contrasting ecosystems. **a,b**, Time series (2011–2012) of plant water storage (L-VOD), TWS, surface soil moisture, rainfall, transpiration, and leaf phenology (LAI) for a 1°×1° area of southeastern US temperate forest (centred at 33.5° N, 85.5° W) (**a**) and African tropical Miombo woodland (centred at 11.5° S, 18.5° E) (**b**). Shading represents s.d. ($n = 16$ for all except TWS, where $n = 3$). The grey shaded rectangles in **b** indicate the dry seasons.

Methods

Datasets. The SMOS satellite has covered the earth surface almost daily with both ascending (6:00) and descending (18:00) overpasses since the beginning of 2010. The whole system underwent a so-called commissioning phase until June 2010, when various operation modes were tested, leading to fewer observations compared with the following years. Therefore, we used data during the period 2011–2016. We selected the ascending observations, as plant water storage usually peaks at dawn. The SMOS-IC algorithm²³ was applied to retrieve L-VOD and soil moisture simultaneously from SMOS observations, without any external vegetation products as inputs, so the current L-VOD retrievals (version 103) were independent of any other vegetation indices. In contrast with other SMOS products (for example, level 2 and level 3)⁵⁰, no remotely sensed LAI data were used in the SMOS-IC retrieval process to estimate L-VOD over heterogeneous pixels, nor were soil moisture data from the European Centre for Medium-Range Weather Forecasts (ECMWF) used to estimate soil moisture over the forest fraction in mixed pixels. The native SMOS spatial resolution (3 dB footprint) varies between ~27 and ~55 km depending on the incidence angles (observations at high incidence angles were filtered out in SMOS-IC). The data were originally projected in the standard EASE-2 grid at a 25 km spatial resolution, and we further converted them into a geographical projection at a 0.25° spatial resolution.

The LAI data were generated from the standard MODerate-resolution Imaging Spectroradiometer (MODIS) Collection 6 LAI products (MOD15 and MYD15; 8-day composites at a 0.05° spatial resolution) from Terra and Aqua for 2011–2016⁵¹. The MODIS LAI algorithm accounts for sun-sensor geometry. We refined the raw LAI data into 16-day composites by averaging the cloud-free observations indicated by the quality flag information to minimize the influences from environmental contamination; for example, clouds, aerosols, shadows and poor sun-sensor geometries. All high-quality LAI data were then resampled to 0.25° by averaging and linearly interpolating to a daily time step to match the spatial and temporal resolutions of the L-VOD data.

The TWS data were from the Gravity Recovery and Climate Experiment (GRACE) satellites, which measure the changes in the Earth's gravitational field that are highly correlated with changes in both surface and subsurface water storage^{52,53}. The monthly GRACE TWS products are provided in three solutions by the GeoForschungsZentrum Potsdam, Centre for Space Research at the University of Texas and Jet Propulsion Laboratory at a 1° spatial resolution. We used the average of the three products and the associated standard deviations, as suggested by recent studies⁵⁴. Only ten observations were available for 2011 and 2012 due to battery management.

The X-VOD data were from the land parameter data record (LPDR version 2) developed by the Numerical Terradynamic Simulation Group at The University of Montana⁵⁵. The X-VOD was retrieved from the Advanced Microwave Scanning Radiometer sensors at a microwave frequency of 10.7 GHz for both ascending (13.30) and descending (1.30) overpasses at a spatial resolution of 0.25°. We selected the descending X-VOD retrievals for 2011–2016. X-VOD was also independent of optical vegetation indices.

The data for tree cover fractions were produced by Chiba University for 2008⁵⁷, since this dataset outperforms the MODIS Vegetation Continuous Fields product (MOD44B) for African drylands where MOD44B largely underestimates the woody cover^{55,56}. Tree height data were from space-borne light detection and ranging data obtained by the Geoscience Laser Altimeter System⁵⁷.

The rainfall data were from the Tropical Rainfall Measurement Mission 3B42 version 7 daily product⁵⁸, which were estimated from satellite measurements at a 0.25° spatial resolution.

The transpiration data were from estimates by the Global Land Evaporation Amsterdam Model version 3.1a, which used a set of algorithms for estimating a series of water cycle components (without plant water storage) at a daily time step and 0.25° spatial resolution^{59,60}.

Analysis of seasonal lag. We concatenated the six-year (2011–2016) data into a mean yearly daily time series for each pixel to obtain a clear and reliable seasonality in L-VOD (see an example pixel in Supplementary Fig. 1a,b). The median of raw L-VOD retrievals from the same day of the year for 2011–2016 was first used to form an average seasonality. Then, a 30-day moving median was determined, followed by calculation of the anomalies between the raw data and the median curve. The data points larger or smaller than the median curve \pm s.d. of the anomalies were defined as outliers and thus removed from the subsequent analysis (de-noise). Finally, a 30-day moving-average curve was calculated for the valid data points. The seasonalities of LAI and X-VOD were determined using the same method as for L-VOD.

For the L-VOD seasonality, we accounted for both the data noise and the actual seasonal variations in plant water storage, using the ratio between the seasonal amplitude and s.d. of the anomalies as an indicator of the intra-annual variability (Supplementary Fig. 1c). Pixels with a ratio >1.2 (a buffer of 20% s.d.) were deemed to be characterized by a clear seasonality, despite the data noise, and were thus selected for further lag analysis with the LAI seasonality. Pixels with a ratio ≤ 1.2 were deemed to have no clear seasonal patterns in L-VOD. Double growing seasons will introduce large uncertainties in quantifying the time lag, so we limited the analysis to pixels characterized by a single growing season in both

L-VOD and LAI seasonality. We normalized the mean seasonality of each pixel to 0–1 by subtracting the minimum value and then dividing by the amplitude, and identified pixels with only two 0.5 crossing points as being characterized by a single growing season⁶¹.

Sensitivity analysis on the L-VOD seasonality. The SMOS-IC algorithm applies a constant soil surface roughness and effective scattering albedo over time and uses an effective temperature input from ECMWF estimates^{23,24}, which will introduce uncertainties in the L-VOD retrievals. We performed a series of sensitivity analyses focusing on the possible influences from these uncertainty settings and sources on the L-VOD seasonal pattern retrieved from the SMOS-IC algorithm over the Miombo region, where L-VOD peaks during the dry season. Specifically, we applied various value settings of these input parameters covering a dynamic range larger than the expected one to examine the possible resulting changes in the L-VOD seasonality.

Soil surface roughness may change in relation to agricultural practices, but this is very unlikely over natural environmental conditions at the satellite footprint scale, such as for the Miombo region. The roughness parameter (HR) used in the SMOS-IC algorithm is 0.3 for the forested pixels in the Miombo region^{62,63}. We compared the L-VOD retrievals over this region by setting HR to 0.2 and 0.4, respectively, but found little difference in the seasonal cycle compared with the setting of 0.3 used in the original SMOS-IC algorithm (Supplementary Fig. 6). Because the seasonal changes in soil surface roughness are expected to be much smaller than an HR range of 0.2, they will have very limited influence on the observed L-VOD seasonal trends.

Canopy leaves have dominant effects on the emissivity and effective scattering albedo of deciduous forests at higher frequencies (>6 GHz), but the leaf effects are limited at the L-band, as suggested by several studies that show that stems and branches are the main elements contributing to forest emissivity at the L-band^{13–15,62}. Therefore, in the SMOS-IC algorithm, a constant effective scattering albedo (Omega) value of 0.06 was used for the Miombo woodlands, which are dominated by a deciduous forest type with a clear annual cycle in canopy leaf conditions^{23,64,65}. To test the influence of an expected small change in the effective albedo (lower than 0.01) on the retrieved L-VOD values, we ran the SMOS-IC algorithm by setting the Omega value to 0.05 and 0.07, respectively, over the Miombo region⁶⁶. Again, the results showed little difference in the retrieved L-VOD seasonal patterns between these different settings (Supplementary Fig. 7). Therefore, using a constant effective scattering albedo of 0.06 in the SMOS-IC algorithm will have a very limited influence on the observed L-VOD seasonal trends over the Miombo woodlands.

The ECMWF soil and vegetation temperatures used to estimate the effective surface temperature (T_s) in the SMOS-IC algorithm⁶⁷ may have a root mean square deviation as high as a few Kelvin^{68,69}. We applied a drastic approach to investigate its possible impacts on the L-VOD seasonal patterns; that is, setting a constant effective temperature (T_s) value over the course of the year. Two constant values (291 and 295 K) with a range of 4 K were considered based on the observed average value (~293 K) and s.d. (~2 K) of seasonal changes in T_s over the Miombo region. Results were compared with L-VOD retrievals considering dynamic ECMWF estimations of T_s , as applied in the SMOS-IC algorithm. Again, little difference in the retrieved L-VOD values from the different T_s settings was observed (Supplementary Fig. 8). This suggests a relatively small impact on L-VOD seasonality from possible uncertainties in the estimates of T_s computed from the ECMWF data, which may be attributable to the narrow seasonal changes in temperature over the Miombo region. Therefore, the uncertainties and possible erroneous trends associated with the ECMWF temperature products cannot explain the specific L-VOD signatures observed in this region.

Analysis of seasonal water balance. A variety of water cycle components were plotted together to investigate the water balance at a US temperate forest site and a tropical Miombo woodland site. Specifically, the SMOS L-VOD and soil moisture data were smoothed using a moving-average method (window size: 30 d). Daily estimates of transpiration were aggregated to a 16-day mean to match the MODIS LAI temporal resolution for better visualization. The onset of the rainy season (or end of the dry season) in the tropical Miombo site was determined following the criteria³⁹: (1) total rainfall of 25 mm within 10 successive days; followed by (2) total rainfall >20 mm within 20 d. The start of the dry season (or end of the rainy season) was defined as the last day with rainfall >10 mm.

Reporting Summary. Further information on experimental design is available in the Nature Research Reporting Summary linked to this article.

Code availability. The code used for seasonal lag analyses in this study has been deposited in GitHub: <https://github.com/fengtian2017/SMOS-L-VOD-seasonality>.

Data availability. SMOS-IC L-VOD seasonality and soil moisture data are available from <https://www.catds.fr/Products/Available-products-from-CEC-SM/SMOS-IC>. MODIS LAI data are available from <http://sites.bu.edu/cliveg>. Anomalous GRACE data for terrestrial groundwater storage are available from <https://grace.jpl.nasa.gov>. X-VOD data can be downloaded from www.ntsg.umt.edu. Tree cover data

are available from <https://globalmaps.github.io/ptc.html>. Tree height data can be downloaded from https://webmap.ornl.gov/ogc/dataset.jsp?ds_id=10023. Tropical Rainfall Measurement Mission rainfall data are available from <https://pmm.nasa.gov>. Transpiration data can be downloaded from <https://www.gleam.eu>. Terrestrial ecoregions data are available at <https://www.worldwildlife.org/publications/terrestrial-ecoregions-of-the-world>.

Received: 13 December 2017; Accepted: 6 July 2018;
Published online: 13 August 2018

References

- Street, H. E. & Cockburn, W. *Plant Metabolism* 2nd edn (Elsevier, Oxford, 1972).
- Sack, L. et al. Plant hydraulics as a central hub integrating plant and ecosystem function: meeting report for 'Emerging Frontiers in Plant Hydraulics' (Washington, DC, May 2015). *Plant Cell Environ.* **39**, 2085–2094 (2016).
- Lin, Y.-S. et al. Optimal stomatal behaviour around the world. *Nat. Clim. Change* **5**, 459–464 (2015).
- De Boer, A. H. & Volkov, V. Logistics of water and salt transport through the plant: structure and functioning of the xylem. *Plant Cell Environ.* **26**, 87–101 (2003).
- Chave, J. et al. Towards a worldwide wood economics spectrum. *Ecol. Lett.* **12**, 351–366 (2009).
- Hartzell, S., Bartlett, M. S. & Porporato, A. The role of plant water storage and hydraulic strategies in relation to soil moisture availability. *Plant Soil* **419**, 503–521 (2017).
- Matheny, A. M. et al. Observations of stem water storage in trees of opposing hydraulic strategies. *Ecosphere* **6**, 1–13 (2015).
- Jones, H. G. Monitoring plant and soil water status: established and novel methods revisited and their relevance to studies of drought tolerance. *J. Exp. Bot.* **58**, 119–130 (2007).
- Wullschleger, S. D., Meinzer, F. C. & Vertessy, R. A. A review of whole-plant water use studies in tree. *Tree Physiol.* **18**, 499–512 (1998).
- Goldstein, G. et al. Stem water storage and diurnal patterns of water use in tropical forest canopy trees. *Plant Cell Environ.* **21**, 397–406 (1998).
- Jackson, T. J. & Schmugge, T. J. Vegetation effects on the microwave emission of soils. *Remote Sens. Environ.* **36**, 203–212 (1991).
- Van de Griend, A. A. & Wigneron, J. P. The b-factor as a function of frequency and canopy type at H-polarization. *IEEE Trans. Geosci. Remote Sens.* **42**, 786–794 (2004).
- Guglielmetti, M. et al. Measured microwave radiative transfer properties of a deciduous forest canopy. *Remote Sens. Environ.* **109**, 523–532 (2007).
- Santi, E., Paloscia, S., Pampaloni, P. & Pettinato, S. Ground-based microwave investigations of forest plots in Italy. *IEEE Trans. Geosci. Remote Sens.* **47**, 3016–3025 (2009).
- Ferrazzoli, P., Guerriero, L. & Wigneron, J. P. Simulating L-band emission of forests in view of future satellite applications. *IEEE Trans. Geosci. Remote Sens.* **40**, 2700–2708 (2002).
- Sternberg, M. & Shoshany, M. Aboveground biomass allocation and water content relationships in Mediterranean trees and shrubs in two climatological regions in Israel. *Plant Ecol.* **157**, 173–181 (2001).
- Jones, M. O., Jones, L. A., Kimball, J. S. & McDonald, K. C. Satellite passive microwave remote sensing for monitoring global land surface phenology. *Remote Sens. Environ.* **115**, 1102–1114 (2011).
- Tian, F. et al. Remote sensing of vegetation dynamics in drylands: evaluating vegetation optical depth (VOD) using AVHRR NDVI and in situ green biomass data over West African Sahel. *Remote Sens. Environ.* **177**, 265–276 (2016).
- Momen, M. et al. Interacting effects of leaf water potential and biomass on vegetation optical depth. *J. Geophys. Res. Biogeosci.* **122**, 3031–3046 (2017).
- Konings, A. G. & Gentine, P. Global variations in ecosystem-scale isohydricity. *Glob. Change Biol.* **23**, 891–905 (2016).
- Konings, A. G., Williams, A. P. & Gentine, P. Sensitivity of grassland productivity to aridity controlled by stomatal and xylem regulation. *Nat. Geosci.* **10**, 284–288 (2017).
- Kerr, Y. H. et al. The SMOS mission: new tool for monitoring key elements of the global water cycle. *Proc. IEEE* **98**, 666–687 (2010).
- Fernandez-Moran, R. et al. SMOS-IC: an alternative SMOS soil moisture and vegetation optical depth product. *Remote Sens.* **9**, 457 (2017).
- Wigneron, J. P. et al. L-band microwave emission of the biosphere (L-MEB) model: description and calibration against experimental data sets over crop fields. *Remote Sens. Environ.* **107**, 639–655 (2007).
- Oliva, R. et al. SMOS radio frequency interference scenario: status and actions taken to improve the RFI environment in the 1400–1427-MHz passive band. *IEEE Trans. Geosci. Remote Sens.* **50**, 1427–1439 (2012).
- Olson, D. M. et al. Terrestrial ecoregions of the world: a new map of life on Earth. *BioScience* **51**, 933–938 (2001).
- Kobayashi, T., Tsend-Ayush, J. & Tateishi, R. A new tree cover percentage map in Eurasia at 500 m resolution using MODIS data. *Remote Sens.* **6**, 209–232 (2014).
- Fluet-Chouinard, E., Lehner, B., Rebelo, L.-M., Papa, F. & Hamilton, S. K. Development of a global inundation map at high spatial resolution from topographic downscaling of coarse-scale remote sensing data. *Remote Sens. Environ.* **158**, 348–361 (2015).
- Rahmoune, R. et al. SMOS retrieval results over forests: comparisons with independent measurements. *IEEE J. Sel. Topics Appl. Earth Observ.* **7**, 3858–3866 (2014).
- Konings, A. G., Piles, M., Das, N. & Entekhabi, D. L-band vegetation optical depth and effective scattering albedo estimation from SMAP. *Remote Sens. Environ.* **198**, 460–470 (2017).
- Morris, H. et al. A global analysis of parenchyma tissue fractions in secondary xylem of seed plants. *New Phytol.* **209**, 1553–1565 (2016).
- Meinzer, F. C., Johnson, D. M., Lachenbruch, B., McCulloh, K. A. & Woodruff, D. R. Xylem hydraulic safety margins in woody plants: coordination of stomatal control of xylem tension with hydraulic capacitance. *Funct. Ecol.* **23**, 922–930 (2009).
- Tyree, M. T. & Sperry, J. S. Vulnerability of xylem to cavitation and embolism. *Annu. Rev. Plant Physiol. Plant Mol. Biol.* **40**, 19–36 (1989).
- Fan, Y., Miguez-Macho, G., Jobbágy, E. G., Jackson, R. B. & Otero-Casal, C. Hydrologic regulation of plant rooting depth. *Proc. Natl Acad. Sci. USA* **114**, 10572–10577 (2017).
- Du, J. et al. A global satellite environmental data record derived from AMSR-E and AMSR2 microwave Earth observations. *Earth Syst. Sci. Data* **9**, 791–808 (2017).
- Tapley, B. D., Bettadpur, S., Ries, J. C., Thompson, P. F. & Watkins, M. M. GRACE measurements of mass variability in the Earth System. *Science* **305**, 503–505 (2004).
- Pokhrel, Y. N., Fan, Y., Miguez-Macho, G., Yeh, P. J. F. & Han, S. C. The role of groundwater in the Amazon water cycle: 3. Influence on terrestrial water storage computations and comparison with GRACE. *J. Geophys. Res. Atmos.* **118**, 3233–3244 (2013).
- Köcher, P., Horna, V. & Leuschner, C. Stem water storage in five coexisting temperate broad-leaved tree species: significance, temporal dynamics and dependence on tree functional traits. *Tree Physiol.* **33**, 817–832 (2013).
- Ryan, C. M., Williams, M., Grace, J., Woollen, E. & Lehmann, C. E. R. Pre-rain green-up is ubiquitous across southern tropical Africa: implications for temporal niche separation and model representation. *New Phytol.* **213**, 625–633 (2017).
- Guan, K. et al. Terrestrial hydrological controls on land surface phenology of African savannas and woodlands. *J. Geophys. Res. Biogeosci.* **119**, 1652–1669 (2014).
- Reich, P. B. Phenology of tropical forests: patterns, causes, and consequences. *Can. J. Bot.* **73**, 164–174 (1995).
- Williams, R. J., Myers, B. A., Muller, W. J., Duff, G. A. & Eamus, D. Leaf phenology of woody species in a north Australian tropical savanna. *Ecology* **78**, 2542–2558 (1997).
- Borchert, R. Soil and stem water storage determine phenology and distribution of tropical dry forest trees. *Ecology* **75**, 1437–1449 (1994).
- Chapotin, S. M., Razanameharizaka, J. H. & Holbrook, N. M. Baobab trees (Adansonia) in Madagascar use stored water to flush new leaves but not to support stomatal opening before the rainy season. *New Phytol.* **169**, 549–559 (2006).
- Trouet, V., Mukelabai, M., Verheyden, A. & Beeckman, H. Cambial growth season of brevi-deciduous *Brachystegia spiciformis* trees from South Central Africa restricted to less than four months. *PLoS ONE* **7**, e47364 (2012).
- Elifuraha, E., Nöjd, P. & Mbwambo, L. Short term growth of Miombo tree species at Kitulungalo. *Work. Pap. Finn. For. Res. Inst.* **98**, 37–45 (2008).
- Domec, J. C. et al. Hydraulic redistribution of soil water by roots affects whole-stand evapotranspiration and net ecosystem carbon exchange. *New Phytol.* **187**, 171–183 (2010).
- Yu, K. & D'Odorico, P. Hydraulic lift as a determinant of tree-grass coexistence on savannas. *New Phytol.* **207**, 1038–1051 (2015).
- Huang, C.-W. et al. The effect of plant water storage on water fluxes within the coupled soil-plant system. *New Phytol.* **213**, 1093–1106 (2017).
- Kerr, Y. H. et al. The SMOS soil moisture retrieval algorithm. *IEEE Trans. Geosci. Remote Sens.* **50**, 1384–1403 (2012).
- Myneni, R. B. et al. Global products of vegetation leaf area and fraction absorbed PAR from year one of MODIS data. *Remote Sens. Environ.* **83**, 214–231 (2002).
- Strassberg, G., Scanlon, B. R. & Chambers, D. Evaluation of groundwater storage monitoring with the GRACE satellite: case study of the High Plains aquifer, central United States. *Water Resour. Res.* **45**, W05410 (2009).
- Reager, J. T. et al. A decade of sea level rise slowed by climate-driven hydrology. *Science* **351**, 699–703 (2016).

54. Sakumura, C., Bettadpur, S. & Bruinsma, S. Ensemble prediction and intercomparison analysis of GRACE time-variable gravity field models. *Geophys. Res. Lett.* **41**, 1389–1397 (2014).
55. Brandt, M. et al. Human population growth offsets climate-driven increase in woody vegetation in sub-Saharan Africa. *Nat. Ecol. Evol.* **1**, 0081 (2017).
56. Brandt, M. et al. Woody plant cover estimation in drylands from Earth Observation based seasonal metrics. *Remote Sens. Environ.* **172**, 28–38 (2016).
57. Simard, M., Pinto, N., Fisher, J. B. & Baccini, A. Mapping forest canopy height globally with spaceborne LIDAR. *J. Geophys. Res. Biogeosci.* **116**, G04021 (2011).
58. Huffman, G. J. et al. The TRMM multisatellite precipitation analysis (TMPA): quasi-global, multiyear, combined-sensor precipitation estimates at fine scales. *J. Hydrometeorol.* **8**, 38–55 (2007).
59. Martens, B. et al. GLEAMv3: satellite-based land evaporation and root-zone soil moisture. *Geosci. Model Dev.* **10**, 1903–1925 (2017).
60. Miralles, D. G. et al. Global land-surface evaporation estimated from satellite-based observations. *Hydrol. Earth Syst. Sci.* **15**, 453–469 (2011).
61. Garonna, I. et al. Strong contribution of autumn phenology to changes in satellite-derived growing season length estimates across Europe (1982–2011). *Glob. Change Biol.* **20**, 3457–3470 (2014).
62. Parrens, M. et al. Global-scale surface roughness effects at L-band as estimated from SMOS observations. *Remote Sens. Environ.* **181**, 122–136 (2016).
63. Fernandez-Moran, R. et al. A new calibration of the effective scattering albedo and soil roughness parameters in the SMOS SM retrieval algorithm. *Int. J. Appl. Earth Obs. Geoinf.* **62**, 27–38 (2017).
64. Vittucci, C., Ferrazzoli, P., Richaume, P. & Kerr, Y. Effective scattering albedo of forests retrieved by SMOS and a three-parameter algorithm. *IEEE Geosci. Remote Sens. Lett.* **14**, 2260–2264 (2017).
65. Parrens, M. et al. Estimation of the L-band effective scattering albedo of tropical forests using SMOS observations. *IEEE Geosci. Remote Sens. Lett.* **14**, 1223–1227 (2017).
66. Du, J., Kimball, J. S. & Jones, L. A. Passive microwave remote sensing of soil moisture based on dynamic vegetation scattering properties for AMSR-E. *IEEE Trans. Geosci. Remote Sens.* **54**, 597–608 (2016).
67. Wigneron, J. P. et al. Modelling the passive microwave signature from land surfaces: a review of recent results and application to the L-band SMOS & SMAP soil moisture retrieval algorithms. *Remote Sens. Environ.* **192**, 238–262 (2017).
68. Holmes, T. R. H., Jackson, T. J., Reichle, R. H. & Basara, J. B. An assessment of surface soil temperature products from numerical weather prediction models using ground-based measurements. *Water Resour. Res.* **48**, W02531 (2012).
69. Albergel, C. et al. Soil temperature at ECMWF: an assessment using ground-based observations. *J. Geophys. Res. Atmos.* **120**, 1361–1373 (2015).

Acknowledgements

We thank E. Fluet-Chouinard, F. Aires and C. Prigent for providing the global inundation map. This work was funded by the CNES through the Science Terre Environment et Climat programme, European Space Agency, Support to Science Element programme and SMOS Expert Support Laboratory. F.T. and R.F. acknowledge funding from the Danish Council for Independent Research (grant ID: DFF-6111-00258). F.T. is also the recipient of the European Union's Horizon 2020 research and innovation programme under the Marie Skłodowska-Curie grant agreement (project number 746347). P.C. and J.P. acknowledge funding from the European Research Council Synergy grant ERC-2013-SyG-610028 IMBALANCE-P. T.T. was funded by the Swedish National Space Board (Dnr: 95/16). P.C. acknowledges additional support from the ANR ICONV CLAND grant. J.C. has benefited from 'Investissement d'Avenir' grants managed by the French Agence Nationale de la Recherche (CEBA (ref. ANR-10-LABX-25-01) and TULIP (ref. ANR-10-LABX-0041)), as well as TOSCA funds from the CNES.

Author contributions

F.T., J.-P.W., M.B. and R.F. designed the study with inputs from P.C., J.C., J.P. and A.R. J.-P.W., Y.K., A.M., N.R.-F. and A.A.-Y. prepared the SMOS-IC data and performed the sensitivity analyses. C.C. and R.B.M. prepared the MODIS LAI data. F.T. performed the data analyses. The results were interpreted by J.-P.W., A.R., J.C., F.T., P.C., J.P., J.O., J.-C.D., X.T., N.R.-F., A.M., T.T., A.A.-Y. and R.F. F.T. drafted the manuscript with editing by P.C., J.P., J.O. and J.C., and contributions from all co-authors.

Competing interests

The authors declare no competing interests.

Additional information

Supplementary information is available for this paper at <https://doi.org/10.1038/s41559-018-0630-3>.

Reprints and permissions information is available at www.nature.com/reprints.

Correspondence and requests for materials should be addressed to F.T. or J.-P.W.

Publisher's note: Springer Nature remains neutral with regard to jurisdictional claims in published maps and institutional affiliations.

Reporting Summary

Nature Research wishes to improve the reproducibility of the work that we publish. This form provides structure for consistency and transparency in reporting. For further information on Nature Research policies, see [Authors & Referees](#) and the [Editorial Policy Checklist](#).

Statistical parameters

When statistical analyses are reported, confirm that the following items are present in the relevant location (e.g. figure legend, table legend, main text, or Methods section).

n/a Confirmed

- The exact sample size (n) for each experimental group/condition, given as a discrete number and unit of measurement
- An indication of whether measurements were taken from distinct samples or whether the same sample was measured repeatedly
- The statistical test(s) used AND whether they are one- or two-sided
Only common tests should be described solely by name; describe more complex techniques in the Methods section.
- A description of all covariates tested
- A description of any assumptions or corrections, such as tests of normality and adjustment for multiple comparisons
- A full description of the statistics including central tendency (e.g. means) or other basic estimates (e.g. regression coefficient) AND variation (e.g. standard deviation) or associated estimates of uncertainty (e.g. confidence intervals)
- For null hypothesis testing, the test statistic (e.g. F , t , r) with confidence intervals, effect sizes, degrees of freedom and P value noted
Give P values as exact values whenever suitable.
- For Bayesian analysis, information on the choice of priors and Markov chain Monte Carlo settings
- For hierarchical and complex designs, identification of the appropriate level for tests and full reporting of outcomes
- Estimates of effect sizes (e.g. Cohen's d , Pearson's r), indicating how they were calculated
- Clearly defined error bars
State explicitly what error bars represent (e.g. SD, SE, CI)

Our web collection on [statistics for biologists](#) may be useful.

Software and code

Policy information about [availability of computer code](#)

Data collection

No software was used.

Data analysis

Data processing were performed by IDL 8.2. The core scripts of time lag analysis are publicly available from GitHub.

For manuscripts utilizing custom algorithms or software that are central to the research but not yet described in published literature, software must be made available to editors/reviewers upon request. We strongly encourage code deposition in a community repository (e.g. GitHub). See the Nature Research [guidelines for submitting code & software](#) for further information.

Data

Policy information about [availability of data](#)

All manuscripts must include a [data availability statement](#). This statement should provide the following information, where applicable:

- Accession codes, unique identifiers, or web links for publicly available datasets
- A list of figures that have associated raw data
- A description of any restrictions on data availability

A data availability statement was presented in the manuscript. All data are either publicly accessible or are available upon request.

Field-specific reporting

Please select the best fit for your research. If you are not sure, read the appropriate sections before making your selection.

Life sciences Behavioural & social sciences Ecological, evolutionary & environmental sciences

For a reference copy of the document with all sections, see [nature.com/authors/policies/ReportingSummary-flat.pdf](https://www.nature.com/authors/policies/ReportingSummary-flat.pdf)

Ecological, evolutionary & environmental sciences study design

All studies must disclose on these points even when the disclosure is negative.

Study description	This study presents the relationship between leaf phenology and whole plant water storage, as measured by L-band vegetation optical depth data retrieved from SMOS satellite at a global scale.
Research sample	We used satellite images cover the entire global land surface, except for large parts of Asia where few or no valid observations were retrieved due to the radio frequency interferences (RFI) impacts on SMOS. The spatial resolution of each satellite sensor determines the number of pixels analyzed in the study.
Sampling strategy	We defined the groups based on existing eco-region maps and tree cover data. We included all the pixels that meet with the criteria, so the sample size is sufficient.
Data collection	The satellite imageries were all collected and provided in their own standard formats.
Timing and spatial scale	The SMOS L-VOD, soil moisture, AMSR X-VOD, TRMM rainfall, and transpiration data were all provided at a 0.25 degree spatial resolution and a daily daily temporal resolution. The VODs have data gaps under frozen soil conditions. MODIS LAI data were provided at a 0.05 degree spatial resolution and a 16-day temporal resolution. GRACE data were provided at a monthly interval and 1 degree spatial resolution. The VODs and LAI data were from 2011-2016, while the others were from 2011-2012.
Data exclusions	We excluded pixels with seasonally inundation events (>5% spatial coverage of a pixel), a sparse vegetation cover (tree cover fraction < 5%), and an annual continuous observations < 120 days, because of the known high-level data uncertainty.
Reproducibility	All the analyses were based on available satellite products and well-defined methods, so the results can be reliably reproduced.
Randomization	Randomization is not apply to this study as we performed wall-to-wall mapping globally with satellite images.
Blinding	Blinding is not relevant for our study as we used well-defined criteria for grouping and included all the valid observations within each group.
Did the study involve field work?	<input type="checkbox"/> Yes <input checked="" type="checkbox"/> No

Reporting for specific materials, systems and methods

Materials & experimental systems

- | n/a | Involvement in the study |
|-------------------------------------|--|
| <input checked="" type="checkbox"/> | <input type="checkbox"/> Unique biological materials |
| <input checked="" type="checkbox"/> | <input type="checkbox"/> Antibodies |
| <input checked="" type="checkbox"/> | <input type="checkbox"/> Eukaryotic cell lines |
| <input checked="" type="checkbox"/> | <input type="checkbox"/> Palaeontology |
| <input checked="" type="checkbox"/> | <input type="checkbox"/> Animals and other organisms |
| <input checked="" type="checkbox"/> | <input type="checkbox"/> Human research participants |

Methods

- | n/a | Involvement in the study |
|-------------------------------------|---|
| <input checked="" type="checkbox"/> | <input type="checkbox"/> ChIP-seq |
| <input checked="" type="checkbox"/> | <input type="checkbox"/> Flow cytometry |
| <input checked="" type="checkbox"/> | <input type="checkbox"/> MRI-based neuroimaging |